Spin-flux skyrmions: Anomalous electron dynamics and spin-Hall currents

Sandip Bera and Sajeev John
Department of Physics, University of Toronto, 60 St. George Street, Toronto, Ontario, Canada M5S 1A7

(Received 30 September 2025; revised 8 December 2025; accepted 14 January 2026; published 6 February 2026)

We introduce a topologically distinct skyrmion, termed a spin-flux skyrmion, which shares the same real-space magnetization profile as a conventional skyrmion but differs fundamentally in its underlying topological structure. This distinction originates from the path traced by its rotation matrices within the doubly connected SO(3) group manifold, leading to a nontrivial spinor phase of $e^{i\pi}$ upon encircling the texture. Using an explicit SU(2) gauge field formalism, we derive the emergent magnetic field components generated by both conventional and spin-flux skyrmions. While conventional skyrmions exhibit a dominant σ_z component with weak dipolar σ_x, σ_y contributions, spin-flux skyrmions possess an additional monopolar σ_x component that yields a finite average emergent field for a finite density of skyrmions. This nontrivial component introduces a nontrivial term in the Hall conductivity, enabling a direct explanation of experimental Hall resistivity anomalies that cannot be accounted for by conventional skyrmions alone. Moreover, we show that this additional term couples to the in-plane spin polarization of conduction electrons, providing a further tunable handle to control the transverse Hall response.

DOI: 10.1103/3l8t-dpn8

I. INTRODUCTION

Magnetic skyrmions are nanoscale spin textures that exhibit a characteristic whirl-like magnetization pattern [1–3], first observed in noncentrosymmetric magnets [4], and later found in many ferromagnetic [5–7] and antiferromagnetic [8] systems. A key property of skyrmions is their integer winding number, often referred to as the skyrmion number, which distinguishes them from other magnetic configurations [7,9]. This number measures how many times the local spin configuration wraps around the unit sphere S^2, as described by a smooth spin texture $\vec{M}(\vec{r})$, over the two-dimensional plane. It is given by $N_{sk} = \frac{1}{4\pi}\int \vec{M}\cdot(\frac{\partial \vec{M}}{\partial x}\times\frac{\partial \vec{M}}{\partial y})dxdy$. A value of $N_{sk} = 1$ corresponds to a single skyrmion, while larger absolute values represent multiple windings, and the sign indicates the sense of rotation of the configuration. Both theoretical and experimental studies have shown that skyrmions can remain stable over a wide range of external magnetic fields, magnetic anisotropy strengths, and temperatures [10–17].

The formation and stability of magnetic skyrmions results from a delicate competition between fundamental magnetic interactions [18,19]. The symmetric Heisenberg exchange interaction (J) favors parallel spin alignment. A crucial ingredient for inducing chirality is the Dzyaloshinskii-Moriya interaction (DMI) (D), an antisymmetric exchange term that favors a fixed, perpendicular canting between neighboring spins [20,21]. This interaction requires broken inversion symmetry, which occurs in noncentrosymmetric crystal lattices. At low or zero external magnetic field, the competition between the DMI and Heisenberg exchange typically produces a one-dimensional spin-spiral (SS) ground state, where the magnetization rotates periodically with a wavelength proportional to J/D. Magnetic anisotropy, such as an easy crystallographic axis for orientation, favors localized magnetic twists, rather than extended spirals. Applying an external magnetic field, which favors spin alignment along the field direction ($+\hat{z}$), likewise stabilizes localized magnetic textures relative to the spin-spiral state. These textures satisfy a well-defined boundary condition: Spins are aligned with the field ($+\hat{z}$) at large distances, while at their core, the spins point opposite to the field ($-\hat{z}$), maintaining a nonzero integer winding number [22]. As the magnetic field strength increases, the ground state evolves predictably. At low fields, the SS phase is stable. With increasing field, the system transitions into a skyrmion lattice phase. At very high fields, the system eventually reaches a fully polarized ferromagnetic (FM) state, in which all spins align with the external field. This sequence of phase transitions has been consistently observed in both theoretical models and experimental studies [10,12–17].

In spintronics, magnetic skyrmions are considered promising candidates for next-generation memory and logic devices due to their stability and nanoscale dimensions [17,23], as well as their controllability by electric currents. Their ability to carry information in a stable, well-defined spin configuration makes them ideal for high-density, low-power-consumption magnetic memory [24,25]. Skyrmions can be driven by current densities 2 to 4 orders of magnitude lower than those required to move conventional magnetic domain walls, typically in the range of $10^6 - 10^8$ A/m^2, compared to $10^{10} - 10^{12}$ A/m^2 for domain wall motion [5,26]. This substantial reduction in current for skyrmion motion, makes them attractive for energy-efficient spintronic devices. For example, skyrmion-based racetrack memory [6,27,28] encodes information in the presence or absence of skyrmions along a narrow magnetic track. Data can be written, shifted, and read by applying short current pulses that move skyrmions, enabling faster data storage and retrieval. This architecture offers high storage density [29,30] while consuming significantly less energy compared to conventional magnetic hard

drives, which rely on moving mechanical parts or high current densities for domain wall motion. Moreover, the high sensitivity of skyrmions to low driving current may enable novel spintronic logic devices [31].

Electron transverse deflection under different Lorentz-like forces leads to various Hall effects. The ordinary Hall effect arises from the Lorentz force of a physical magnetic field acting on charge carriers. In contrast, the anomalous Hall effect occurs in ferromagnetic materials with magnetic textures due to intrinsic spin-orbit coupling, even without an external magnetic field [32]. In materials hosting skyrmions, the spatial variation of magnetization gives rise to a synthetic matrix magnetic field, strongest near the skyrmion cores. This field deflects conduction electrons, producing a transverse voltage. The resulting contribution to the Hall signal is referred to as the *skyrmion-induced Hall effect* [6,7].

In this article, we introduce a topologically distinct skyrmion that superficially exhibits the same magnetization profile as the conventional Néel skyrmion. The topological distinction arises from the detailed set of rotation matrices used to form the magnetic texture and the path traced by the rotation matrices, within the SO(3) group manifold of physical rotations in three-dimensional space, as the skyrmion is encircled by a path in two-dimensional coordinate space (Fig. 1). It is well known that the group manifold of SO(3) is topologically, doubly connected. It has been suggested [33,34] that this is the fundamental reason for the existence of spin $-1/2$ particles. It enables the two-valued nature of the spin $-1/2$ wave function and that under a 2π rotation, the wave function changes sign. It is the doubly connected nature of SO(3) that allows this two-valued wave function to be everywhere continuous and differentiable. We refer to this distinctive magnetic soliton as a spin-flux skyrmion. As in the case of conventional skyrmions, the effects of the spin-flux skyrmion on a conduction electron can be described by a matrix gauge field whose matrix components can be represented by the set of Pauli spin matrices $\{\sigma_x, \sigma_y, \sigma_z\}$. A fundamental consequence of the spin-flux skyrmion is that when an electron encircles this texture it acquires a nontrivial phase of $e^{i\pi}$. It has been suggested that nontrivial and consequential spin-flux may play a vital role in high-temperature cuprate superconductors [34–38].

Superfluid ^{3}He-A is another physical system in which an SO(3) order parameter space has been discussed. Here, Cooper pairs form in a p-wave orbital angular momentum and spin triplet wave function. This spin-1 condensate exhibits interesting topological structures such as vortices and half-vortices [39,40]. However, they do not rely on the doubly connected nature of SO(3). Our spin-flux skyrmion is constituted of spin-1/2 electrons. The underlying wave function, leading to its observable magnetic moment structure, involves constituent electrons that undergo a 2π rotation in their internal coordinate frame as the electron encircles the skyrmion core.

In this paper, we focus on the explicit form of the SU(2) gauge field for spin-flux skyrmions and highlight its distinctive features compared to conventional skyrmions. For conventional skyrmions, the σ_z component of the emergent magnetic field is dominant, peaking at the skyrmion core and rapidly decaying with increasing radius, while the σ_x and σ_y components exhibit a weaker dipolar distribution, with a peak magnitude approximately one quarter of that of σ_z. In contrast, spin-flux skyrmions exhibit a qualitatively different behavior: the σ_z component retains a similar radial profile, but a highly consequential σ_x component appears, with a singular monopolar character. This monopolar feature leads to a finite contribution to the average emergent field in a skyrmion lattice, a property absent in the conventional case. Consequently, the emergent magnetic field introduces an additional term in the Hall conductivity, supplementing the diagonal contribution common to both skyrmion types. This additional term provides a natural explanation for certain experimental observations that cannot be captured by the conventional skyrmion model alone. Furthermore, we demonstrate how the spin polarization density matrix of electrons driven by an electric field can be used to control the Hall current in the presence of spin-flux skyrmions.

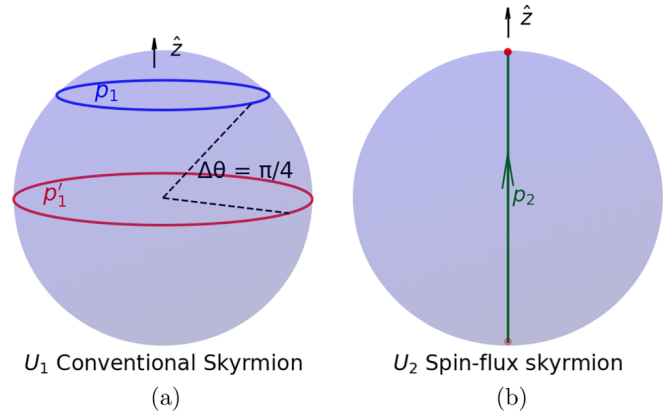

FIG. 1. We illustrate the distinction between two skyrmions corresponding to magnetic moment rotation fields U_1 and $U_2 = U_2^z U_2^y$, in terms of the SO(3) group manifold [panels (a) and (b)]. In this picture, a solid ball of radius π is used to represent all possible spin rotations: each point inside the ball corresponds to a unique rotation, the displacement from the origin indicates the rotation angle, and the direction specifies the rotation axis. The surface of the ball therefore represents a rotation angle of π. For the conventional U_1 skyrmion [panel (a)], we consider circular paths in coordinates space with radii $r = \rho_0$ (the skyrmion core radius) and $r = \infty$, which we label as p_1 and p_1', respectively. All rotation matrices describing this skyrmion configuration lie infinitesimally below the surface of the SO(3) ball (shown in blue and red). Here, the rotation field corresponds to a fixed rotation angle of π about the spatially varying axis unit vector $\hat{n}(\vec{r})$. As the skyrmion is encircled, the spin rotation trajectory in SO(3) forms a closed loop on the surface. Both paths, p_1 and p_1', can be continuously deformed to a single point and are considered topologically trivial within SO(3). For the U_2(spin-flux) skyrmion [panel (b)], the rotation U_2^y corresponds to single point in SO(3) on the y axis for any circular path of given radius. The rotation U_2^z traverses a straight line path from the surface of SO(3), through the center of the ball, to the antipodal point as the skyrmion is encircled at any radius and $-\pi < \zeta < \pi$. This endows the U_2-skyrmion with a nontrivial spin-flux of π. Since antipodal points on the sphere of radius π are identical rotations, the path p_2 cannot be continuously deformed to a single point. In other words, the paths $p_1(p_1')$ and p_2 are homotopically distinct.

II. EMERGENT MAGNETIC FIELD GOVERNING SKYRMION-ELECTRON INTERACTION

A. Topological distinctions

The interaction between skyrmions and electrons arises due to the coupling between the spin of conduction electrons and the local magnetization of the skyrmion texture. This interaction can be effectively described by an exchange coupling term in the Hamiltonian, where the conduction electron spin $\vec{\sigma}$ interacts with the local magnetization $\vec{M} = (\sin\theta\cos\phi, \sin\theta\sin\phi, \cos\theta)$ of the skyrmion via $H_{\text{int}} = -J_h\vec{M}\cdot\vec{\sigma}$, and J_h is the exchange interaction strength [41–46]. The orientation angles θ and ϕ are functions of the planar polar coordinates r and ζ, representing radial distance from the origin and angle to the x coordinate axis, respectively. In most systems, the ferromagnetic Hund's coupling ($J_h > 0$) aligns conduction-electron spins parallel to the local magnetization [47,48]. When the spins are aligned, the coordinate space wave function vanishes if the two electrons come very close to one another, thereby reducing the Coulomb repulsion energy. The strength of the skyrmion-electron interaction, J_h, typically ranges from 1 to 100 meV [46,49], and plays a crucial role in transport and scattering of electrons in skyrmion-hosting environments. A minimal nonrelativistic Hamiltonian describing the itinerant electrons whose spins are coupled to the localized moments is $H = \frac{\vec{P}^2}{2m} - J_h\vec{M}\cdot\vec{\sigma}$, where $\vec{P}$ is the momentum operator of the free electron. This can be reexpressed as an electron effectively coupled to a uniform ferromagnet, but experiencing effective SU(2) gauge forces. We write $\psi = U^\dagger(\boldsymbol{r})\Psi$, where Ψ is the spinor in the laboratory frame and ψ is the spinor in the locally rotated frame, varying from point to point in coordinate space. The SU(2) transformation matrix $U(\boldsymbol{r})$ is chosen such that $U^\dagger(\boldsymbol{M}\cdot\boldsymbol{\sigma})U = \sigma_z$, thereby aligning the local spin quantization axis with the local magnetization $\boldsymbol{M}(\boldsymbol{r})$. In this gauge-transformed frame, the spinor is expressed as $\psi = \binom{\psi_+}{\psi_-}$, where ψ_+ and ψ_- correspond to electronic states with spin locally aligned and antialigned with $\boldsymbol{M}$, respectively. This unitary matrix $U(\boldsymbol{r}, t)$, which can also vary with time for a nonstatic magnetic background, encodes all the information about the rotation of the spin basis at each point in the spin texture.

A simple representation of the matrix field is given by $U(\boldsymbol{r}) = e^{i\boldsymbol{\sigma}\cdot\epsilon(\boldsymbol{r})}$, where σ are the Pauli matrices, and $\epsilon(\boldsymbol{r})$ is a position-dependent vector encoding the spin rotation parameters. For rotation about a fixed axis, defined by a unit vector $\hat{n}$ and by angle θ, $\epsilon(\boldsymbol{r}) = \theta\hat{n}/2$. Importantly, the choice of $U(\boldsymbol{r})$ is not unique. Different gauge choices correspond to different ways of defining the local spin frame while still satisfying the condition in $U^\dagger(\boldsymbol{M}\cdot\boldsymbol{\sigma})U = \sigma_z$. As we show below, there are two different types of SU(2) unitary matrix fields that can represent the same local magnetic moment field of a skyrmion. This dichotomy arises from the doubly connected topology of the SO(3) group manifold, which describes physical rotations in three-dimensional space. There are two homotopically distinct classes of paths within SO(3). Paths within one class cannot be continuously deformed to paths within the second class. The group manifold of SO(3) can be represented as a solid ball of radius π. Each point in this manifold corresponds to unique rotation matrix. A rotation by an angle θ about an axis $\hat{n}$ is located at a displacement, θ, from the origin of the solid ball in the direction of $\hat{n}$. Rotation by angle π is the same as a rotation by angle $-\pi$, so the antipodal points of the solid ball are identified to be the same point. In other words, two distinct SU(2) matrices correspond to the same physical rotation. The leads to the doubly connected topology of the manifold. There are two distinct classes of matrix fields $U(\boldsymbol{r})$ that can be chosen to represent the magnetic moment structure of the skyrmion. For the conventional skyrmion, as the coordinate vector, $\vec{r}$, encircles the skyrmion, the matrices $U_1(\vec{r})$ form a path, p_1, within SO(3) that does not cross the surface of the solid ball of radius π. This is depicted in Fig. 1. In contradistinction, a spin-flux carrying skyrmion is generated by the matrix field $U_2(\vec{r})$ with a path, p_2, within SO(3) that cannot be continuously deformed to p_1 within the doubly connected topological manifold of SO(3). The two paths in SO(3) are homotopically inequivalent because the path p_2 crosses the surface of the solid ball of radius π, whereas the path p_1 does not.

Applying the SU(2) transformation field to the electron Hamiltonian, $H' = U^\dagger(\boldsymbol{r})H(\boldsymbol{r})U(\boldsymbol{r})$, modifies the momentum operator as $\vec{P} \to \vec{P} + \vec{\mathcal{A}}$, where the emergent matrix gauge potential is given by $\vec{\mathcal{A}} = -i\hbar U^\dagger\nabla U$, and $\mathcal{A}_0 = i\hbar U^\dagger\partial_t U$. In our case of static skyrmions, $\mathcal{A}_0 = 0$ since U is time independent. This leads to a synthetic matrix magnetic field that influences electron dynamics in a manner similar to the Lorentz force in electrodynamics. However, the SU(2) gauge field, unlike the conventional electrodynamic vector potential, introduces a spin-dependent force. The freedom in choosing topologically distinct (homotopically nonequivalent) sets of matrices $U(\boldsymbol{r})$ leads to fundamentally and consequentially different gauge potentials. As we show below, the choice $U_2(\vec{r})$ (corresponding to a spin-flux carrying skyrmion) leads to an SU(2) gauge field that is singular as $r \to 0$. An electron encircling this skyrmion at a large distance from its core acquires a nontrival phase of $e^{i\pi}$ as if the skyrmion carries a magnetic solenoid containing a flux of π. On the other hand, the choice $U_1(\boldsymbol{r})$ (corresponding to a conventional skyrmion) yields a nonsingular gauge field. An electron encircling this skyrmion acquires a trivial phase of $e^{2i\pi}$. These two topologically distinct skyrmions exhibit identical local magnetic moment distributions, but lead to different dynamics for the itinerant electron.

The synthetic magnetic field of a single $U_1(\boldsymbol{r})$ skyrmion has a monopolar structure in the σ_z component, but a dipolar structure in the σ_x and σ_y component (see Fig. 2). In the presence of uniform density of such skyrmions, there is a nonzero average value of the net magnetic field for the σ_z component. However, the average magnetic field for the σ_x and σ_y components vanishes due to the canceling effects of different dipoles. In contrast, the synthetic magnetic field of a single $U_2(\vec{r})$ spin-flux skyrmion has a monopolar structure in both the σ_z and σ_x components (see Fig. 3). For a uniform density of $U_2(\boldsymbol{r})$ spin-flux skyrmions, there is a nonzero average value of the synthetic magnetic field for both the σ_z and σ_x components. This leads to observable differences in the electron dynamics in the presence of $U_1(\boldsymbol{r})$ vs. $U_2(\boldsymbol{r})$ skyrmion densities.

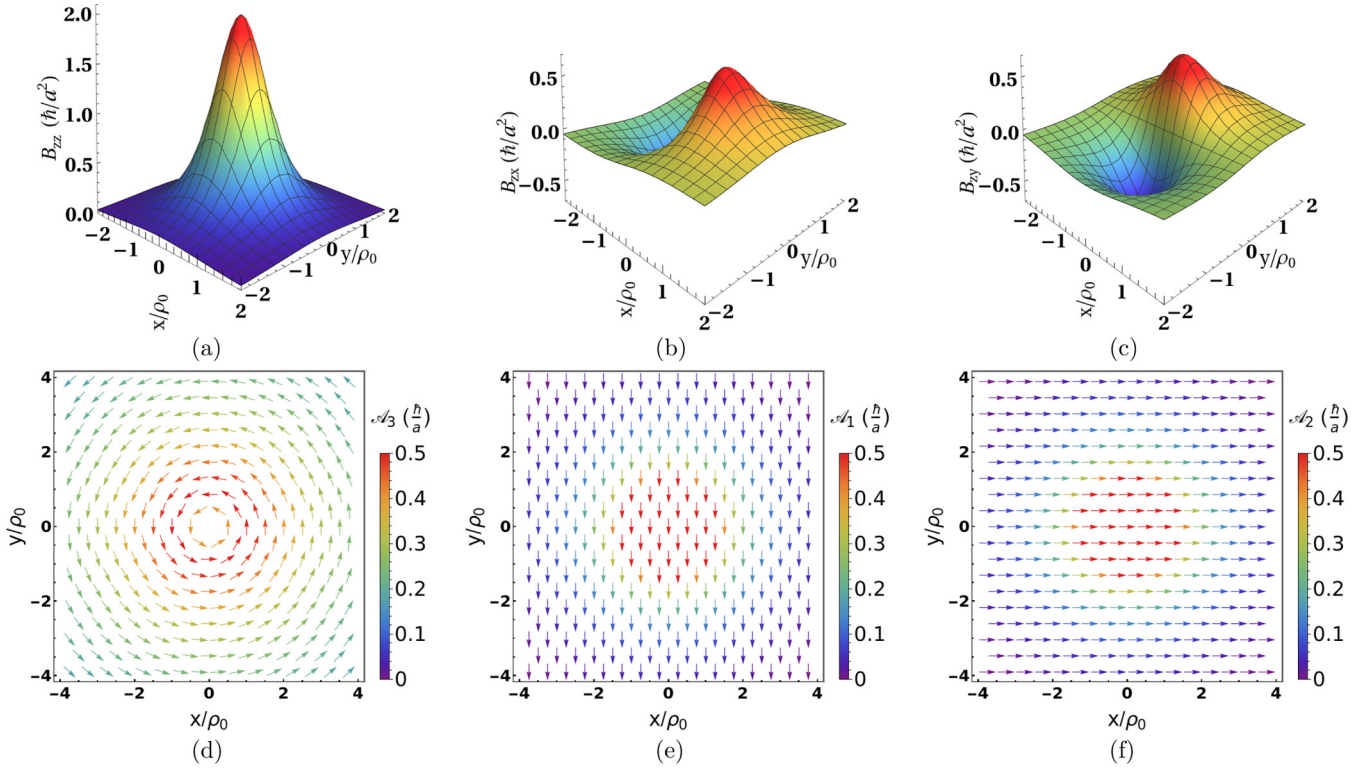

FIG. 2. Behavior of the emergent magnetic field and vector potential for a conventional Néel skyrmion with spin rotation $\theta(r) = 2\tan^{-1}(r/\rho_0)$, and $U_1 = \exp(-i\frac{\pi(\hat{n}\cdot\vec{\sigma})}{2})$, where $\vec{n} = (\sin\frac{\theta}{2}\cos\phi, \sin\frac{\theta}{2}\sin\phi, \cos\frac{\theta}{2})$. Panels (a–c) display the σ_z, σ_x, and σ_y components of the magnetic field, respectively. Panels (d–f) show the corresponding components of the vector potential. The color bars represent the magnitude of the vector potential, while the arrows indicate its direction. The emergent vector potential and magnetic field are scaled in units of $\hbar/a$ and $\hbar/a^2$, respectively, where a is the lattice constant.

In the literature, a commonly adopted form of the SU(2) unitary transformation $U_1(\boldsymbol{r})$ is [46,50]

$$U_1(\boldsymbol{r}) = \exp\left(-i\frac{\pi(\hat{n}\cdot\vec{\sigma})}{2}\right). \tag{1}$$

Here, the unit vector $\vec{n} = (\sin\frac{\theta}{2}\cos\phi, \sin\frac{\theta}{2}\sin\phi, \cos\frac{\theta}{2})$ defines the axis of rotation and the angles θ and ϕ are functions of 2D polar coordinates r and ζ. This transformation corresponds to a single rotation by angle π about the axis $\hat{n}$, which lies halfway between the local magnetization direction and the z axis. As a result, $U_1(\boldsymbol{r})$ rotates the local spin texture into alignment with the z axis. The rotational path traced out by such transformations within the SO(3) group manifold, as $\vec{r}$ encircles the skyrmion, dictates key features of the emergent gauge potential. Two example paths, p_1 and p_1', within SO(3) are depicted in Fig. 1(a), corresponding to circles of different radii (in coordinate space) that encircle the skyrmion.

Instead of the commonly used unitary matrix form, an alternative form of the $U(\boldsymbol{r})$ matrix was introduced in Ref. [34], which is topologically distinct from $U_1(\boldsymbol{r})$ but yields the same magnetic textures. In particular, the unitary matrix $U_2(\boldsymbol{r})$ follows a sequence of two separation rotations:

$$U_2(\boldsymbol{r}) = \exp\left(-i\frac{\sigma_z\zeta}{2}\right)\exp\left(-i\frac{\sigma_y\theta(r)}{2}\right). \tag{2}$$

The skyrmion defined by the rotation matrix field $U_2(\boldsymbol{r})$ exhibits the same topological charge, defined by the mapping $\mathbb{R}^2 \to S^2$, as the conventional skyrmion. However, $U_2(\boldsymbol{r})$ defines a homotopically distinct path within the group manifold of SO(3) from $U_1(\boldsymbol{r})$ as the electron encircles the skyrmion in coordinate space. As we show below, this leads to observable differences in electron dynamics between these distinct skyrmions. The unitary matrix product $U_2 = U_2^z U_2^y$ again aligns the electron spin with the local magnetization at each point in space. The factor, $U_2^y \equiv \exp(-i\frac{\sigma_y\theta}{2})$, describes the rotation by an angle θ around the y axis, aligning the spinor with the local magnetization direction in the yz plane. The factor, $U_2^z \equiv \exp(-i\frac{\sigma_z\zeta}{2})$, applies a rotation by an angle, $\phi = \zeta$, around the z axis. The path followed by the rotations U_2^z in the group manifold of SO(3) as the skyrmion is encircled is depicted in Fig. 1(b). The skyrmion involving U_2^z exhibits a consequential "spin-flux" of π causing spin-dependent destructive wave interference of two electron trajectories passing either side of the skyrmion core.

The effective gauge potential $\vec{\mathcal{A}}$ modifies the electron motion similarly to a real magnetic vector potential except in a spin-dependent manner. This can be described by the emergent field $\vec{B} = \nabla \times \vec{\mathcal{A}}$. One consequence of this emergent field is the topological Hall effect (THE), where electrons experience a transverse Lorentz force due to their interaction with the skyrmion. The transformed Hamiltonian $H' = \frac{1}{2m}(\boldsymbol{P} + \boldsymbol{A})^2 - J_h\sigma_z$ now includes an emergent SU(2) gauge potential $\boldsymbol{A}$. Depending on the homotopically distinct choices of the unitary matrix fields, U_1 or U_2, the structure of the

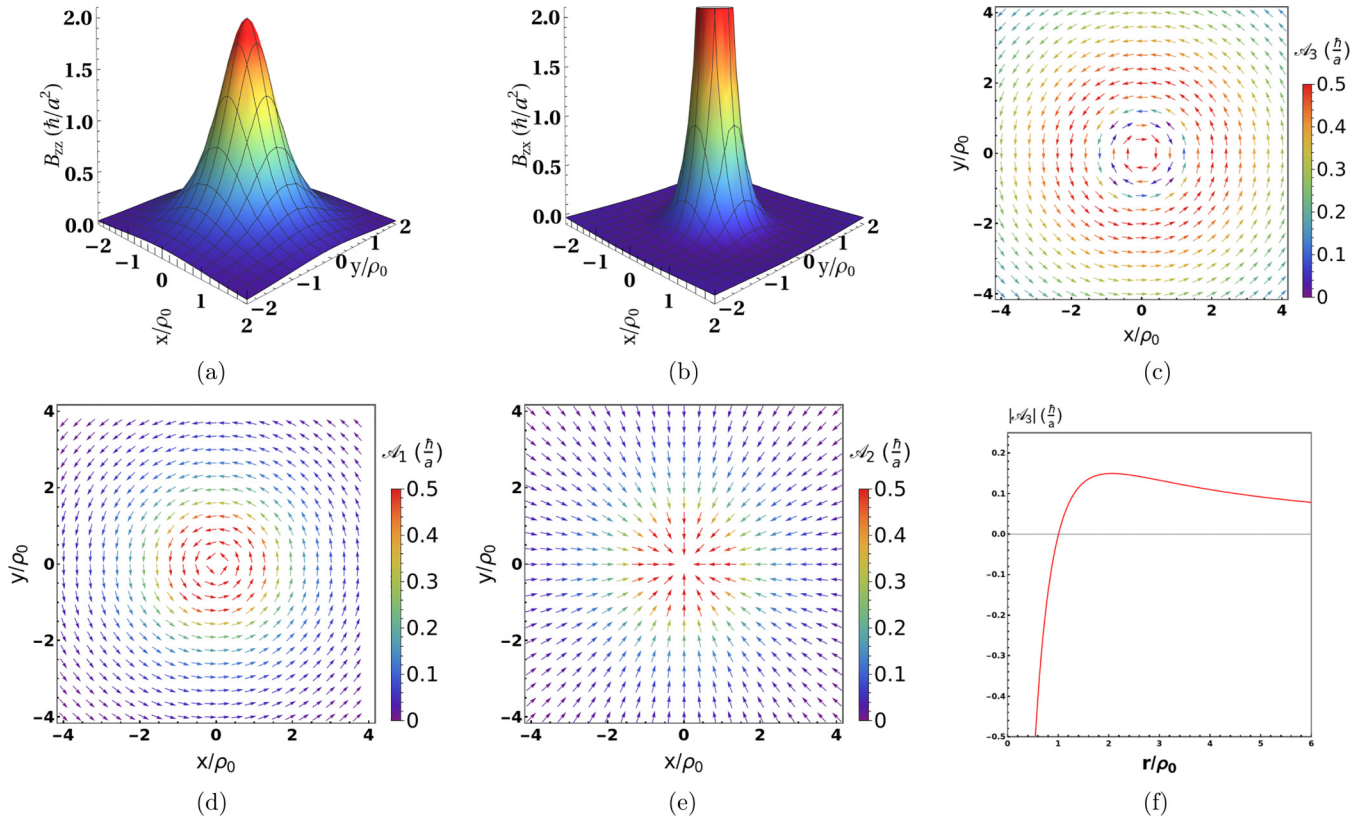

FIG. 3. The emergent magnetic field and vector potential for a spin-flux skyrmion with $\theta(r) = 2\tan^{-1}(r/\rho_0)$, and unitary matrix field $U_2 = e^{-i\frac{\sigma_z\zeta}{2}} e^{-i\frac{\sigma_y\theta(r)}{2}}$. Panels (a) and (b) show the σ_z and σ_x components of the emergent magnetic field, respectively. Notably, the σ_y component vanishes in this configuration. Unlike U_1, an emergent off-diagonal magnetic field of monopolar form appears in the σ_x component. Panels (c–e) display the σ_z, σ_x, and σ_y components of the vector potential. The color bars represent the magnitude of the vector potential, while the arrows indicate its direction. Panel (f) shows the singular radial dependence of the σ_z component of the vector potential, denoted as $\mathcal{A}_3$. The emergent vector potential and magnetic field are scaled in units of $\hbar/a$ and $\hbar/a^2$, respectively, where a is the lattice constant.

emergent gauge potential and its associated physical consequences differ. In the next section, we analyze the explicit forms of the SU(2) gauge potentials produced by a single skyrmion. In particular, the skyrmion created by $U_2(\boldsymbol{r})$ exhibits monopolar off-diagonal components in its emergent magnetic field and a vector potential similar to that of a magnetic solenoid carrying a magnetic flux of π. In our analysis, we treat the skyrmion as a static texture.

B. Synthetic gauge field due to conventional skyrmions

The local magnetization $\boldsymbol{M} = (\sin\theta\cos\phi, \sin\theta\sin\phi, \cos\theta)$, is defined at each point $\boldsymbol{r} = (x, y) \equiv (r\cos\zeta, r\sin\zeta)$, where r is the radial distance from the origin and ζ is the angle with respect to the x axis. The angles θ and ϕ are functions of r and ζ. For the U_1 unitary matrix, the emergent gauge vector potential is given by (see Appendix A)

$$\vec{\mathcal{A}} = \frac{\hbar}{2}\Big[\theta_r(\sigma_y\cos\phi - \sigma_x\sin\phi)\hat{r} + \hat{\zeta}\,\frac{2\phi_\zeta\sin\frac{\theta}{2}}{r}\left(\sigma_z\sin\frac{\theta}{2} - \cos\frac{\theta}{2}(\sigma_x\cos\phi + \sigma_y\sin\phi)\right)\Big], \tag{3}$$

where $\theta_r \equiv \partial\theta/\partial r$ and $\phi_\zeta \equiv \partial\phi/\partial\zeta$. Here, $\hat{r}$ is the unit vector in the radial direction and $\hat{\zeta}$ is the unit vector in the azimuthal direction. We consider a skyrmion whose central spin is aligned along the $+z$ direction, with a radially outward rotation described by $\theta(r) = 2\tan^{-1}(r/\rho_0)$. In all our calculations, we consider only Néel-type skyrmions, for which $\phi = \zeta$ [6,10]. In this case, the detailed form of the emergent vector potential and the corresponding emergent magnetic field are (see Appendix A 1 for details)

$$\begin{aligned}\vec{\mathcal{A}} &= \frac{\hbar}{2}\Big[\frac{2\rho_0}{r^2+\rho_0^2}(\sigma_y\cos\zeta - \sigma_x\sin\zeta)\hat{r} \\ &\quad + \hat{\zeta}\left(\sigma_z\frac{2r}{r^2+\rho_0^2} - \frac{2\rho_0}{r^2+\rho_0^2}(\sigma_x\cos\zeta + \sigma_y\sin\zeta)\right)\Big] \\ &\equiv \sigma_x\vec{\mathcal{A}}_1 + \sigma_y\vec{\mathcal{A}}_2 + \sigma_3\vec{\mathcal{A}}_3 \end{aligned} \tag{4}$$

$$\begin{aligned}B_z &= \hbar\left[\sigma_z\frac{2\rho_0^2}{\left(r^2+\rho_0^2\right)^2} + \frac{2r\rho_0}{\left(r^2+\rho_0^2\right)^2}(\sigma_x\cos\zeta + \sigma_y\sin\zeta)\right] \\ &\equiv \sigma_z B_{zz} + \sigma_x B_{zx} + \sigma_y B_{zy}. \end{aligned} \tag{5}$$

The behavior of σ_z, σ_x, and σ_y components of the vector potential are shown in Figs. 2(d), 2(e), and 2(f), respectively. Here, the arrows indicate the direction of the vector potential

at each point, while the colored bars represent its magnitude. As shown in Fig. 2(d), the σ_z component of the vector potential is maximal at the skyrmion center and decays as $1/r$ at large distances. In contrast, σ_x and σ_y components, shown in Figs. 2(e) and 2(f), decay more rapidly, following a $1/r^2$ dependence. Additionally, the maximum value of the σ_z component is approximately 1.4 that of the other two components. Since the σ_z component of $\mathcal{A}$ is aligned along the azimuthal direction, it contributes directly to the magnetic flux. On the other hand, σ_x and σ_y components are aligned purely along the y and x directions, respectively, and do not produce net magnetic flux. The total magnetic flux enclosed within a circle of radius $\mathcal{R}$ is given in Eq. (6). In the limit $\mathcal{R} \to \infty$, this total flux approaches 2π. The flux experienced by an up-spin electron is opposite to that of a down-spin electron. Since the vector potential lies in the x-y plane it generates only a z component of synthetic SU(2) magnetic field.

The explicit form of this fictitious magnetic field is given in Eq. (5). The σ_z component of the magnetic field, denoted B_{zz}, is maximum at the center of the skyrmion and decays as $1/r^4$ with distance. The behavior of B_{zz} in the $x-y$ plane is shown in Fig. 2(a). Among all components, B_{zz} has the highest magnitude-approximately four times larger than the B_{zx} and B_{zy} components depicted in Figs. 2(b) and 2(c), respectively. The B_{zx} component exhibits an antisymmetric dipolar structure along the x axis resulting in zero net magnetic flux over the skyrmion area. The B_{zy} component shows a similar dipolar profile along the y axis, also contributing no net magnetic flux. For this conventional (nonsingular) skyrmion:

$$\begin{aligned}\oint_C \vec{\mathcal{A}} \cdot d\vec{l} &\equiv \int_{-\pi}^{\pi} \vec{\mathcal{A}}(\mathcal{R},\zeta)\cdot\hat{\zeta}\mathcal{R}d\zeta \\ &= 2\pi\hbar\left(1-\frac{\rho_0^2}{\mathcal{R}^2+\rho_0^2}\right)\sigma_z \\ &= 2\pi\hbar\sigma_z|_{\mathcal{R}\to\infty} \end{aligned} \tag{6}$$

$$\begin{aligned}\int_S B_z dxdy &\equiv \int_0^{\mathcal{R}}\int_{-\pi}^{\pi} B_z(r,\zeta) r dr d\zeta \\ &= 2\pi\hbar\left(1-\frac{\rho_0^2}{\mathcal{R}^2+\rho_0^2}\right)\sigma_z \\ &= 2\pi\hbar\sigma_z|_{\mathcal{R}\to\infty}. \end{aligned} \tag{7}$$

Here, the line integral is taken along a circular contour C of radius $\mathcal{R}$, and the surface integral extends over the circular dis k $S : 0 \leqslant r \leqslant \mathcal{R}, -\pi \leqslant \zeta \leqslant \pi$.

C. Singular gauge field due to spin-flux skyrmions

The general expression for the SU(2) gauge potential associated with a U_2 spin-flux skyrmion is given by (see Appendix A)

$$\vec{\mathcal{A}} = \frac{\hbar}{2}\left[-\theta_r\sigma_y\hat{r} + \frac{\hat{\zeta}\phi_\zeta}{r}(-\sigma_z\cos\theta + \sigma_x\sin\theta)\right]. \tag{8}$$

We again consider a representative up-center skyrmion configuration defined by $\theta(r) = 2\tan^{-1}(r/\rho_0)$, and $\phi = \zeta$. For this choice, the explicit analytical forms of the emergent gauge potential and the corresponding SU(2) magnetic field exhibit singularities as $r \to 0$ (see Appendix A 2 for details):

$$\begin{aligned}\vec{\mathcal{A}} = \frac{\hbar}{2}\Bigg[&-\frac{2\rho_0}{\rho_0^2+r^2}\sigma_y\hat{r} \\ &+\hat{\zeta}\left(-\sigma_z\frac{\rho_0^2-r^2}{r\left(\rho_0^2+r^2\right)}+\sigma_x\frac{2\rho_0}{\rho_0^2+r^2}\right)\Bigg] \end{aligned} \tag{9}$$

$$B_z = \hbar\left[\sigma_z\frac{2\rho_0^2}{\left(\rho_0^2+r^2\right)^2}+\frac{\rho_0\left(\rho_0^2-r^2\right)}{r\left(\rho_0^2+r^2\right)^2}\sigma_x\right]. \tag{10}$$

The behaviors of the σ_z, σ_x, and σ_y components of the vector potential are illustrated in Figs. 3(c), 3(d), and 3(e), respectively. Here, the arrows indicate the direction of the vector at each point, and the colored bars represent the magnitude of the vector potential. The σ_z component of the vector potential exhibits a $1/r$ singularity at the center of the skyrmion and decays as $1/r$ for larger. The other two components are nonsingular as $r \to 0$ and decay as $1/r^2$ at large distances. Both σ_z and σ_x components are aligned along the azimuthal direction, contributing to the total magnetic flux. The explicit form of the flux inside a circle of radius $\mathcal{R}$ is given in Eq. (12). Unlike the case discussed in Sec. II B, where the magnetic flux originates solely from the σ_z component, the U_2 skyrmion exhibits flux contributions from both σ_z and σ_x. As shown in Fig. 3(f), the σ_z component of the azimuthal vector potential [see Eq. (9)] changes sign at $r = \rho_0$. For $r < \rho_0$, this component is negative, resulting in a clockwise circulation of the vector field. For $r > \rho_0$, it becomes positive, reversing the rotation direction to counterclockwise [see Fig. 3(c)]. This is a distinctive behavior for U_2-skyrmion not present in the U_1-skyrmion. In the limit $\mathcal{R} \to \infty$, the total magnetic flux approaches 2π. However, the line integral of the vector potential approaches π leading to distinct phase changes from the U_1-skyrmion as the electron encounters the U_2-skyrmion. An electron encircling the U_2 skyrmion acquires a nontrivial phase factor of $e^{i\pi}$. For this reason, we refer to the U_2 skyrmion as a "spin-flux" skyrmion. The usual Stoke's theorem, relating magnetic flux to the line integral of the vector potential, is inapplicable due to the singular form of the gauge field as $r \to 0$.

The explicit form of the fictitious magnetic field for the U_2 spin-flux skyrmion is given in Eq. (10). The σ_z component of the magnetic field, denoted by B_{zz}, reaches its maximum at the center of the skyrmion, as shown in Fig. 3(a). This behavior closely resembles that observed for the U_1 skyrmion discussed earlier. In contrast, the B_{zx} component of the U_2 spin-flux skyrmion, shown in Fig. 3(b), exhibits a unique structure. Unlike the dipolar pattern observed in the U_1-skyrmion, the B_{zx} field now displays a singular monopolelike structure centered at the skyrmion core and also decays as $1/r^3$ for large distances. For the (singular) spin-flux skyrmion:

$$\begin{aligned}\int B_z dxdy &= 2\pi\hbar\left[\left(1-\frac{\rho_0^2}{\mathcal{R}^2+\rho_0^2}\right)\sigma_z+\frac{\mathcal{R}\rho_0}{\mathcal{R}^2+\rho_0^2}\sigma_x\right] \\ &= 2\pi\hbar\sigma_z|_{\mathcal{R}\to\infty} \end{aligned} \tag{11}$$

$$\begin{aligned}\oint \vec{\mathcal{A}}\cdot d\vec{l} &= 2\pi\hbar\left[\left(\frac{1}{2}-\frac{\rho_0^2}{\mathcal{R}^2+\rho_0^2}\right)\sigma_z+\frac{\mathcal{R}\rho_0}{\mathcal{R}^2+\rho_0^2}\sigma_x\right] \\ &= \pi\hbar\sigma_z|_{\mathcal{R}\to\infty}. \end{aligned} \tag{12}$$

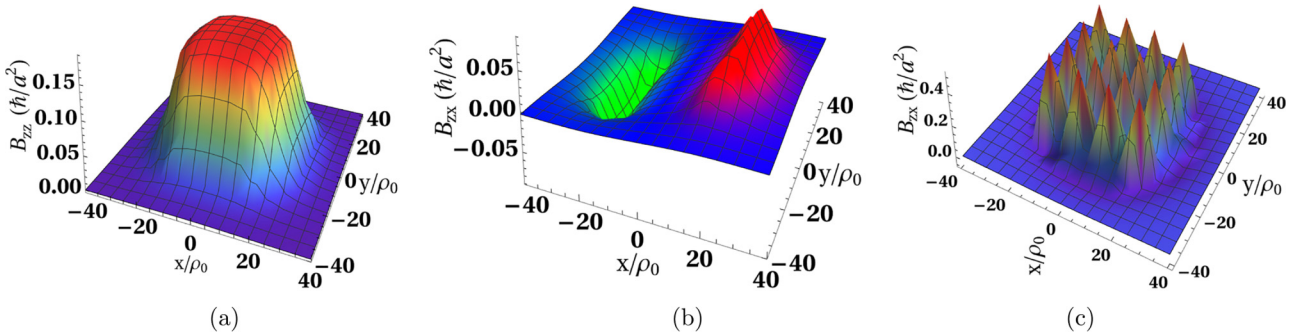

FIG. 4. Spatial profiles of components of the emergent magnetic field, for a lattice of skyrmions with core radius $\tilde{\rho}_0 = 5a$, within the large circular region of radius $\tilde{r} = 20a$. Panel (a) shows the distribution of the B_{zz} component in the $x - y$ plane for a lattice of either U_1 or U_2 skyrmions. For both skyrmion lattices, B_{zz} remains nearly uniform throughout the interior but drops sharply near the boundary. Panel (b) presents the spatial variation of B_{zx} for the U_1 skyrmion lattice. As expected, B_{zx} is nearly zero across the central area but becomes nonzero near the boundary and displays a dipolarlike structure. In contrast, panel (c) illustrates the behavior of B_{zx} for the U_2 skyrmion lattice. This has monopolar peaks at the center of each skyrmion, leading to a significant average value over the large circular area.

D. Average field of a skyrmion lattice

We now consider a periodic arrangement of skyrmions confined within a large circular region of radius r_0, as illustrated in Fig. 6(c). Here, we assume that the presence of multiple skyrmions can be represented by a linear superposition of their emergent gauge fields. The total emergent magnetic field is obtained by summing the contributions from all individual skyrmions within this region as depicted in Fig. 4. For the σ_z component, the total field for both the U_1- skyrmion and the U_2- skyrmion is given by

$$B_{zz}^{\text{total}} = \sum_i B_{zz}^i = \sum_i \frac{2\rho_0^2\hbar}{\left[\left(x - x_0^i\right)^2 + \left(y - y_0^i\right)^2 + \rho_0^2\right]^2}. \quad (13)$$

Here, (x_0^i, y_0^i) are the coordinates of the center of the i^{th} skyrmion, and πr_0^2 is the total area of the skyrmion region. The total number of skyrmions is N_t, and the skyrmion density is defined as $D_{sk} = \frac{N_t}{\pi r_0^2}$. To obtain the average magnetic field, we integrate the total field over the system area. For the σ_z component, the average is given by $B_{zz}^{av} = \frac{1}{\pi r_0^2}\int B_{zz}^{total} dxdy$. The average values of the other components, B_{zx}^{av} and B_{zy}^{av}, can be computed similarly and we denote the matrix average as $B_z^{av} = B_{zx}^{av}\sigma_x + B_{zy}^{av}\sigma_y + B_{zz}^{av}\sigma_z$. In what follows, we generalize B_z^{av} to represent a configuration average, $[B_z]_c$, over different skyrmion coordinate locations [not restricted to those depicted in Fig. 6(c)]. We assume that $[B_z]_c = B_z^{av}$. The average emergent magnetic field components, B_{zz}^{av} and B_{zx}^{av}, are functions of skyrmion density and radius. As shown in Fig. 5(a), B_{zz}^{av} increases with skyrmion density for both U_1- and U_2-type skyrmions. Conversely, Fig. 5(b) shows that B_{zz}^{av} decreases with increasing skyrmion core radius ρ_0. This highlights the competing roles of skyrmion size and density in determining the spatially averaged field.

The off-diagonal components B_{zx} and B_{zy} of the emergent magnetic field of a conventional skyrmion (U_1) exhibit dipolelike structures oriented along the x and y directions, respectively, as illustrated in Fig. 2. Consider a crystal of skyrmions filling a large circular region [see Fig. 6(c)]. In such a configuration, the dipole field of one skyrmion can overlap with that of a nearby skyrmion, leading to partial or complete cancellation of the local field in the interior region. In any event, the spatial averages the off-diagonal components of the emergent field of the U_1- skyrmion crystal cancel out in the bulk of the system. However, this cancellation does not hold at the boundaries if the dipolar fields are aligned in one direction.

This situation is quite different for a lattice of U_2-skyrmions. Figure 5(c) shows that the average emergent field component B_{zx}^{av} increases with skyrmion density. As shown in Fig. 5(d), B_{zx}^{av} initially increases with skyrmion radius ρ_0, but eventually saturates. This behavior can be understood from the monopolar nature of the emergent field of a single skyrmion $B_{zx}(r) \propto \frac{\rho_0(\rho_0^2 - r^2)}{r(\rho_0^2 + r^2)^2}$, which is singular at the skyrmion center and decays as $1/r^3$ for $r \gg \rho_0$. This distinctive behavior provides a framework for interpreting certain experimental results on the Hall conductivity as a function of applied magnetic field, as we discuss below (see Fig. 8).

In summary, for the U_1-skyrmion, the spatially averaged emergent magnetic field component B_{zz}^{av} increases with skyrmion density but decreases with skyrmion core radius, while the off-diagonal components B_{zx}^{av} and B_{zy}^{av} are negligibly small. In contrast, for the U_2 spin-flux skyrmion, both B_{zz}^{av} and B_{zx}^{av} are significant, with B_{zx}^{av} increasing with skyrmion core radius. Thus, the averaged emergent matrix magnetic fields for a finite density of skyrmions takes the form

$$B_z^{av} = \begin{cases} B_{zz}^{av}\sigma_z, & \text{for } U_1 \text{ (Conventional skyrmions)} \\ B_{zz}^{av}\sigma_z + B_{zx}^{av}\sigma_x, & \text{for } U_2 \text{ (Spin-flux skyrmions)} \end{cases}. \quad (14)$$

This contributes to different dynamics for an itinerant electron encountering a region of U_1- skyrmions vs. U_2- skyrmions even in a semiclassical picture, as demonstrated in Sec. III.

III. SPIN-DEPENDENT DRUDE THEORY

We now consider the semiclassical dynamics of an electron subject to the emergent matrix-valued magnetic field generated by a finite density of skyrmions. In this framework, fluctuations of the emergent field around its average value are treated as an additional scattering source, contributing to an effective relaxation time τ. The resulting transport behavior is

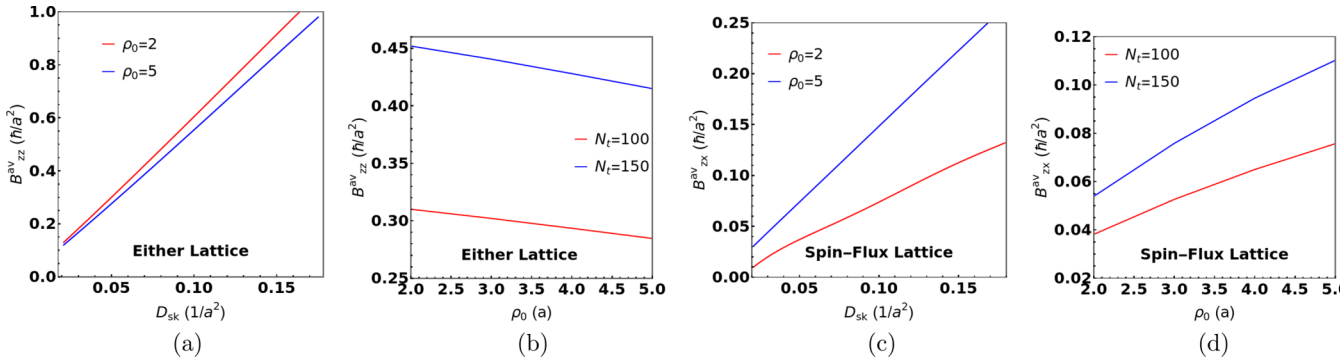

FIG. 5. Panels (a) and (b) show the behavior of the averaged magnetic field component $B^{\rm av}_{zz}$ as a function of skyrmion density, $D_{\rm sk}$, and skyrmion radius ρ_0, respectively. $B^{\rm av}_{zz}$ remains the same for both U_1- skyrmion and spin-flux U_2- skyrmion lattices. Panels (c) and (d) display the behavior of the averaged off-diagonal field component $B^{\rm av}_{zx}$ for U_2- skyrmion lattice, as a function of $D_{\rm sk}$ and ρ_0, respectively. The amplitude of $B^{\rm av}_{zz}$ is larger than that of $B^{\rm av}_{zx}$, due to their distinct functional forms, as described in Eqs. (5) and (10). The dependence of $B^{\rm av}_{zz}$ and $B^{\rm av}_{zx}$ on ρ_0 is qualitatively different as seen by comparing panels (b) and (d). For the U_1- skyrmion lattice, the average values of the off-diagonal field components are nearly zero. In all cases, the region containing skyrmions has a radius of $25a$, where a is the lattice spacing between magnetic moments.

described using a spin-dependent generalization of the Drude model [51]. We start from an effective Heisenberg equation of motion for the electron momentum operator:

$$m\dot{\vec{v}} = -q\vec{E}\sigma_0 - m\frac{\vec{v}}{\tau} - B_z(\vec{v}\times\hat{z}). \tag{15}$$

Here $\vec{v} = \hat{x}\dot{x} + \hat{y}\dot{y}$ is the velocity operator, which includes the identity matrix, σ_0, in spin space. Here, $\vec{E}$ is the physical external electric field, and B_z represents the spin-dependent emergent magnetic field arising from a finite density of stationary skyrmions. The term $B_z(\vec{v}\times\hat{z})$ is a spin-dependent Lorentz-like force due to this emergent field, while the damping term $m\frac{\vec{v}}{\tau}$ phenomenologically accounts for momentum relaxation from impurities, emergent-field fluctuations, and other sources of random scattering. A detailed derivation is presented in Appendix B. The first term on the right-hand side corresponds to the force exerted by the external electric field, acting identically on all spin states. The Drude-like equation (15) gives rise to spin-selective transport determined by the specific form of the conduction electron spin density matrix.

We now take the ensemble average and quantum expectation value of Eq. (15) under steady-state conditions, where the average acceleration vanishes, i.e., $\langle\dot{\vec{v}}\rangle_{\rm ens} = 0$. Assuming a uniform applied electric field along the x axis, the spin-dependent Drude equation reduces to the following Cartesian component:

$$0 = -qE_x - m\frac{\langle v_x\rangle_{\rm ens}}{\tau} - \langle B_z v_y\rangle_{\rm ens}. \tag{16}$$

Here, the ensemble average $\langle\hat{O}\rangle_{\rm ens}$ for any operator $\hat{O}$ is defined as $\langle\hat{O}\rangle_{\rm ens} = [\langle\hat{O}\rangle]_c$, where $[\hat{O}]_c$ denotes a configurational average over skyrmion positions, and $\langle\hat{O}\rangle \equiv {\rm Tr}(\rho\,\hat{O})$ is the quantum mechanical expectation value with respect to the

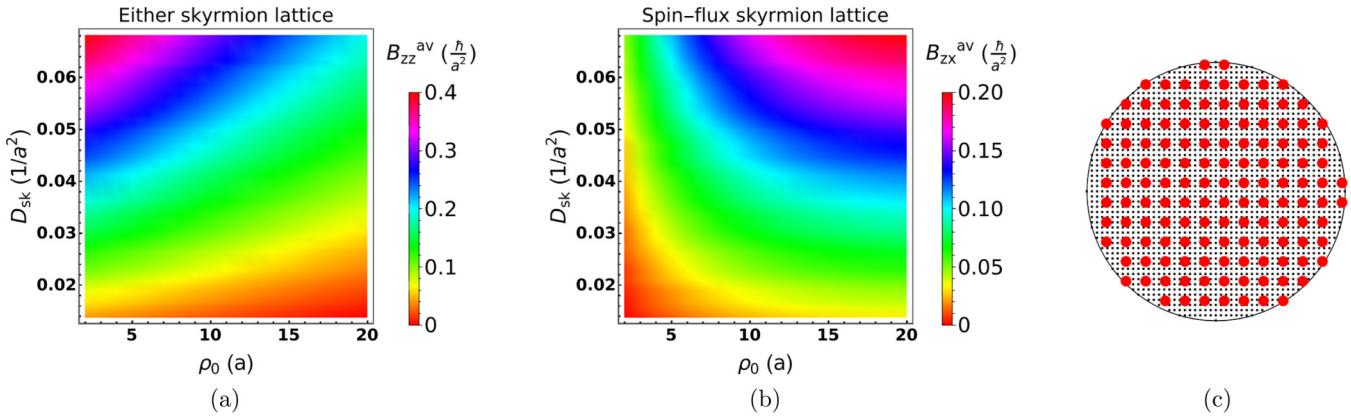

FIG. 6. Panel (a) depicts the averaged magnetic field component $B^{\rm av}_{zz}$(identical for both U_1- skyrmions and U_2 spin-flux skyrmions) as a function of skyrmion density $D_{\rm sk}$ and skyrmion radius ρ_0. The color bar indicates the magnitude of $B^{\rm av}_{zz}$. Panel (b) displays the distribution of the $B^{\rm av}_{zx}$ component for the U_2 spin-flux skyrmion in the same parameter space. Clearly, $B^{\rm av}_{zz}$ increases with skyrmion density but decreases with increasing skyrmion radius. In contrast, $B^{\rm av}_{zx}$ is nonzero and large only in U_2 skyrmions. This shows a monotonic increase with both skyrmion density and radius. Panel (c) shows a schematic representation of skyrmions arranged in a square lattice within a large circle of radius $\tilde{r}_0 = 25a$. The red dots denote individual skyrmions, while black dots mark the underlying lattice sites of individual magnetic moments. The radius of each skyrmion is set to $\tilde{\rho}_0 = 2a$.

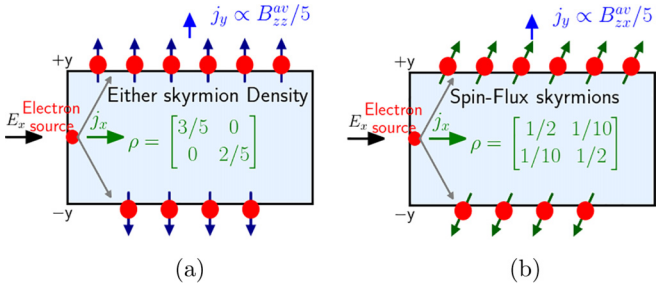

FIG. 7. Cartoon illustration of the transverse Hall effect from a density of conventional and spin-flux skyrmions. (a) For a current composed of 60% electrons with $\langle\sigma_z\rangle = +1$ (upward arrows) and 40% with $\langle\sigma_z\rangle = -1$ (downward arrows), electrons with $\langle\sigma_z\rangle = +1$ deflect toward the $+y$ edge, while those with $\langle\sigma_z\rangle = -1$ accumulate at the $-y$ edge. The resulting Hall current originates from the average $B_{zz}^{\rm av}$ component of the emergent field and is identical for both conventional and spin-flux skyrmions. (b) For a current composed of 60% electrons with $\langle\sigma_x\rangle = +1$ (oblique right arrows) and 40% with $\langle\sigma_x\rangle = -1$ (oblique left arrows), the Hall response arises from the average $B_{zx}^{\rm av}$ component. For this input current, a finite Hall current arises only from a density of spin-flux skyrmions, while a density of conventional skyrmions yields no transverse response.

conduction electron density matrix ρ. This formulation ensures that both the spatial distribution of skyrmions and the quantum spin state of conduction electrons are consistently taken into account when evaluating transport quantities. In the regime where the applied electric field is strong and the influence of the emergent magnetic field is weak, the longitudinal electron dynamics is primarily governed by the electric field and the relaxation time τ. Under this assumption, the term $\langle B_z v_y\rangle_{\rm ens}$ can be neglected, and the steady-state longitudinal velocity simplifies to

$$\langle v_x\rangle_{\rm ens} \approx -\frac{\tau q}{m} E_x. \tag{17}$$

For the transverse (y) direction, Eq. (15) reduces to $0 = -m\frac{\langle v_y\rangle_{\rm ens}}{\tau} + \langle B_z v_x\rangle_{\rm ens}$. Substituting Eq. (17) for $\langle v_x\rangle_{\rm ens}$ into Eq. (16) and applying a mean-field factorization $\langle B_z v_x\rangle_{\rm ens} \approx \langle B_z\rangle_{\rm ens}\langle v_x\rangle_{\rm ens}$, we obtain the approximate transverse velocity:

$$\begin{aligned}\langle v_y\rangle_{\rm ens} &\approx \frac{\tau}{m}\langle B_z\rangle_{\rm ens}\langle v_x\rangle_{\rm ens} \\ &= -\frac{q\tau^2}{m^2} E_x \langle B_z^{\rm av}\rangle,\end{aligned} \tag{18}$$

where $B_z^{av} \equiv [B_z]_c$ denotes the configurationally averaged emergent magnetic field. The corresponding longitudinal current is $j_x \equiv -qn\langle v_x\rangle_{\rm ens} = \frac{n\tau q^2}{m} E_x \equiv \sigma_{xx} E_x$, where $\sigma_{xx} = \frac{n\tau q^2}{m}$ is the conventional Drude longitudinal conductivity and n is the carrier density. The transverse (Hall) current $j_y \equiv -qn\langle v_y\rangle_{\rm ens} = \frac{nq^2\tau^2}{m^2} E_x \langle B_z^{\rm av}\rangle \equiv \sigma_{yx} E_x$, with the Hall conductivity given by

$$\sigma_{yx} = \begin{cases} \frac{nq^2\tau^2}{m^2} B_{zz}^{\rm av} \langle\sigma_z\rangle, & \text{for } U_1 \text{ (Conventional skyrmions)}, \\ \frac{nq^2\tau^2}{m^2}\left[B_{zz}^{\rm av}\langle\sigma_z\rangle + B_{zx}^{\rm av}\langle\sigma_x\rangle\right], & \text{for } U_2 \text{ (Spin-flux skyrmions)}. \end{cases} \tag{19}$$

This result reveals that the Hall conductivity depends explicitly on the spin expectation values of the input current and the emergent magnetic field generated by the skyrmion lattice, leading to a spin-polarized topological Hall effect. For U_1 skyrmions, the Hall signal arises solely from the out-of-plane component $\langle\sigma_z\rangle$, consistent with earlier reports [7,52–56]. In contrast, for U_2 skyrmions, an additional in-plane term proportional to $\langle\sigma_x\rangle$ emerges due to the finite $B_{zx}^{\rm av}$ component. A summary of the differences between conventional and spin-flux skyrmions is presented in Table I.

To illustrate this quantitatively, consider a conduction electron population described by the spin density matrix $\rho = \left(\begin{smallmatrix} 3/5 & 0 \\ 0 & 2/5 \end{smallmatrix}\right)$, which corresponds to an incoherent mixture of 60% electrons with $\langle\sigma_z\rangle = +1$ (spin-up) and 40% electrons with $\langle\sigma_z\rangle = -1$ (spin-down). In other words, $n_\uparrow = 0.60n$ and $n_\downarrow = 0.40n$, where $n = n_\uparrow + n_\downarrow$ is the total carrier density. From Eq. (19), the emergent field B_{zz}^{av} deflects spin-up electrons toward the $+y$ direction and spin-down electrons toward the $-y$ direction with equal transverse velocity magnitude v_y.

TABLE I. Comparison of key properties between conventional skyrmions and spin-flux skyrmions, including the Unitary matrix, the form of the emergent magnetic field, the phase obtained from the line integral of the gauge potential over a closed loop of radius $\mathcal{R}$, the average field for a skyrmion lattice, and the expression of the spin-dependent Hall conductivity.

Key Feature	Conventional skyrmion	Spin-flux skyrmion
Unitary matrix	$U_1 = e^{-i\frac{\pi(\hat{n}\cdot\vec{\sigma})}{2}}$.	$U_2 = e^{-i\frac{\sigma_z\zeta}{2}} e^{-i\frac{\sigma_y\theta(r)}{2}}$.
Emergent field B_z	$\hbar\left[\sigma_z \frac{2\rho_0^2}{(r^2+\rho_0^2)^2} + \frac{2r\rho_0}{(r^2+\rho_0^2)^2}(\sigma_x\cos\zeta + \sigma_y\sin\zeta)\right]$	$\hbar\left[\sigma_z \frac{2\rho_0^2}{(\rho_0^2+r^2)^2} + \frac{\rho_0(\rho_0^2-r^2)}{r(\rho_0^2+r^2)^2}\sigma_x\right]$
$\oint_C \vec{\mathcal{A}}\cdot d\vec{l}$	$2\pi\hbar\left(1 - \frac{\rho_0^2}{\mathcal{R}^2+\rho_0^2}\right)\sigma_z$	$2\pi\hbar\left[\left(\frac{1}{2} - \frac{\rho_0^2}{\mathcal{R}^2+\rho_0^2}\right)\sigma_z + \frac{\mathcal{R}\rho_0}{\mathcal{R}^2+\rho_0^2}\sigma_x\right]$
B_z^{av}	$B_{zz}^{av}\sigma_z$	$B_{zz}^{av}\sigma_z + B_{zx}^{av}\sigma_x$
σ_{yx}	$\frac{nq^2\tau^2}{m^2} B_{zz}^{\rm av}\langle\sigma_z\rangle$	$\frac{nq^2\tau^2}{m^2}\left[B_{zz}^{\rm av}\langle\sigma_z\rangle + B_{zx}^{\rm av}\langle\sigma_x\rangle\right]$

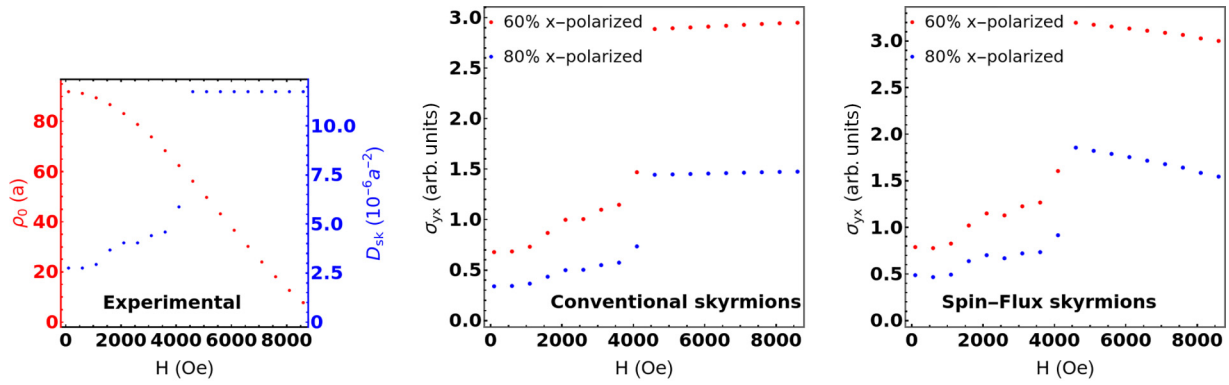

FIG. 8. Panel (a) shows extracted experimental data from Ref. [57], giving the skyrmion core radius (ρ_0) and the skyrmion density (D_{sk}) as a function of external magnetic field. The experimental D_{sk} increases from $2.5 \times 10^{-6}a^{-2}$ to $11.5 \times 10^{-6}a^{-2}$ as the field is increased. To simulate such densities we utilize a circular region of radius $1317a$. Using the experimental data from (a), we compute the field dependence of the Hall conductivity using Eq. (19). The configuration averaged emergent fields are calculated using the recipe illustrated in Fig. 5. Panel (b): For conventional skyrmions, the Hall conductivity increases rapidly with field up to the point where the skyrmion density saturates, and then continues to increase slowly due to the gradual reduction of the skyrmion radius. Panel (c): For spin-flux skyrmions, the Hall conductivity first rises rapidly with field but, after the density saturates, decreases with increasing field. This decrease originates from the finite B_{zx} component of the emergent field and reproduces the experimental trend reported in Ref. [57]. In panels (b) and (c), we consider two choices of the input current. In the first case, an incoherent mixture of 40% $\langle\sigma_z\rangle = 1$ and 60% $\langle\sigma_x\rangle = 1$ is assumed (red dots), while in the second case 20% $\langle\sigma_z\rangle = 1$ and 80% $\langle\sigma_x\rangle = 1$ is used (blue dots). The slope of the conductivity decrease depends on the relative weights of in-plane and out-of-plane spin components. The σ_{yx} scale on the y axis is the same for panels (b) and (c).

The resulting transverse *charge* current density is then

$$\begin{aligned} j_y &= -q(n_\uparrow < v_{y,\uparrow} >_{\text{ens}} + n_\downarrow < v_{y,\downarrow} >_{\text{ens}}) \\ &= \frac{q^2\tau^2}{m^2} B_{zz}^{\text{av}} E_x (n_\uparrow - n_\downarrow) \\ &= \frac{1}{5}\frac{n q^2\tau^2}{m^2} B_{zz}^{\text{av}} E_x. \end{aligned} \tag{20}$$

This applies to both U_1 and U_2 skyrmion densities, as illustrated in Fig. 7(a).

Alternatively, consider a conduction electron population consisting of an incoherent mixture with 60% of electrons polarized along $+\hat{x}$ ($\langle\sigma_x\rangle = +1$) and 40% along $-\hat{x}$ ($\langle\sigma_x\rangle = -1$). The corresponding spin density matrix is $\rho = \left(\begin{smallmatrix} 1/2 & 1/10 \\ 1/10 & 1/2 \end{smallmatrix}\right)$, expressed in the σ_z basis. In the σ_x basis, $n_+ = 0.60n$ and $n_- = 0.40n$, where $n = n_+ + n_-$ is the total carrier density. The emergent magnetic field B_{zx}^{av} now deflects $\langle\sigma_x\rangle = +1$ electrons in the $+y$ direction and $\langle\sigma_x\rangle = -1$ electrons in the $-y$ direction, both with equal transverse velocity magnitude v_y. The resulting transverse *charge* current density is

$$\begin{aligned} j_y &= -q(n_+ < v_{y,+} >_{\text{ens}} + n_- < v_{y,-} >_{\text{ens}}) \\ &= \frac{q^2\tau^2}{m^2} B_{zx}^{\text{av}} E_x (n_+ - n_-) \\ &= \frac{1}{5}\frac{n q^2\tau^2}{m^2} B_{zx}^{\text{av}} E_x. \end{aligned} \tag{21}$$

This contribution is unique to the U_2 (spin-flux) skyrmions, since B_{zx}^{av} is absent in conventional U_1 skyrmions. In other words, a finite Hall response under in-plane spin polarization provides a direct experimental signature for the presence of spin-flux skyrmions, as illustrated in Fig. 7(b).

Experimental results are often reported in terms of the Hall resistivity ρ_{yx}. This is related to the conductivity through the tensor inversion formula $\rho_{yx} = \frac{\sigma_{yx}}{\sigma_{xx}^2 + \sigma_{yx}^2}$. In the small Hall angle limit (as also noted in Ref. [57]), where $|\sigma_{yx}| \ll \sigma_{xx}$, this reduces to $\rho_{yx} \approx \frac{\sigma_{yx}}{\sigma_{xx}^2}$. Since σ_{xx} is approximately constant with the external magnetic field, the field dependence of ρ_{yx} closely follows that of σ_{yx}, differing only by a scaling factor. In this case σ_{yx} can be compared to experimentally observed variations of ρ_{yx} with an externally applied magnetic field. It has been shown [10,13] that an external magnetic field controls the density and the core radii of the magnetic skyrmions.

In Ref. [57], for the material system $[\text{Ta/CoFeB/MgO}]_{1.5}$, the measured topological Hall conductivity increases with magnetic field, reaches a maximum, and then decreases. From the same study, we extract the field dependence of both the skyrmion core radius (ρ_0) and the skyrmion density (D_{sk}), as shown in Fig. 8(a). The experimentally observed D_{sk} increases from $2.5 \times 10^{-6}a^{-2}$ to $11.5 \times 10^{-6}a^{-2}$ (with $a = 0.29$ nm) as the external magnetic field is increased from 0 to 4500 Oe, and then D_{sk} remains nearly constant over the field range 4500–8500 Oe. In order to simulate this behavior, we model a circular region of radius $1317a$ to maintain a total skyrmion number and density, D_{sk}, consistent with the experimentally observed values [Fig. 8(a)]. Using our model, we compute the average emergent fields. For a given applied magnetic field, each pair of data points in Fig. 8(a) can be associated with a single point in either Fig. 6(a) or 6(b). As the applied magnetic field is varied continuously, it describes paths in Figs. 6(a) and 6(b), from which the emergent magnetic fields as a function of applied magnetic field is determined. Inserting these emergent fields into our analytical framework [Eq. (19)], we calculate the Hall conductivity for both conventional and spin-flux skyrmions, as shown in Figs. 8(b) and 8(c). This is

done for two choices of the input current. In the first case, we consider an incoherent mixture of 40% $\langle\sigma_z\rangle = 1$ and 60% $\langle\sigma_x\rangle = 1$, with electron spin density-matrix $\rho_1 = \left(\begin{smallmatrix}0.7 & 0.3\\ 0.3 & 0.3\end{smallmatrix}\right)$. In the second case, an incoherent mixture of 20% $\langle\sigma_z\rangle = 1$ and 80% $< \sigma_x >= 1$, with electron spin density-matrix $\rho_2 = \left(\begin{smallmatrix}0.6 & 0.4\\ 0.4 & 0.4\end{smallmatrix}\right)$.

Figure 8(b) shows the behavior of σ_{yx} with external magnetic field for conventional skyrmions, evaluated for the two density matrices, ρ_1 (red dots) and ρ_2 (blue dots). The initial increase of σ_{yx} with magnetic field is well known from the literature [7,24,58,59], corresponding to the formation and growth of the skyrmion phase. In both cases, σ_{yx} increases rapidly with magnetic field, and then continues to rise only slowly once the skyrmion density saturates. This trend arises because both the emergent field component B_{zz} and the skyrmion density increase with magnetic field. After the density becomes nearly constant, σ_{yx} is controlled primarily by the shrinking skyrmion core radius. Since conventional skyrmions only possess a finite B_{zz} component, the resulting Hall conductivity never decreases with field but instead shows a gradual saturation. However, in the experimental data of Ref. [57], a clear downturn of σ_{yx} is observed before the final high-field collapse. This intermediate-field reduction is not simply explained by conventional skyrmion models [7,24,58,60]. Our spin-flux skyrmion mechanism provides a simple, natural, and fundamental explanation. At sufficiently high magnetic fields (in this case above ∼8500 Oe), the skyrmion density sharply decreases as the system approaches a phase transition into either the conical or the ferromagnetic phase. Experimentally, this leads to a rapid collapse of the topological Hall signal, as observed in Ref. [57]. This high-field collapse is widely reported [7,24,56,60–63] and can be understood with both conventional and spin-flux skyrmions.

In contrast, for spin-flux skyrmions [Fig. 8(c)], both B_{zz} and B_{zx} components contribute. Initially, σ_{yx} again increases with field due to the rising skyrmion density. However, once the density saturates, the conductivity is determined by the core radius: B_{zz} decreases with radius [see Fig. 5(b)], while B_{zx} increases [see Fig. 5(d)]. Their combined effect in Eq. (19) produces a nonmonotonic σ_{yx}, which decreases after reaching a maximum. The rate of decrease depends sensitively on the relative spin composition of the conduction electrons. Specifically, a larger fraction of in-plane spins enhances the relative weight of the B_{zx} contribution, which counterbalances the B_{zz} term and leads to faster drop in σ_{yx}. This effect is evident in Fig. 8(c), where the blue dots denote results for ρ_2 and red symbols for ρ_1. For ρ_2, σ_{yx} decreases more rapidly because of the stronger in-plane spin polarization. The resulting field dependence of σ_{yx} in our spin-flux model resembles the experimental trend reported in Ref. [57], where σ_{yx} increases at low fields, peaks, and then decreases. Such nonmonotonic behavior of σ_{yx} with applied magnetic field is not explained by conventional skyrmions alone. Similar behavior of the experimentally observed the Hall resistivity with external magnetic field is reported in other materials, including FeGe [61,62], MnSi [56,59], MnGe [64], $GdRu_2Ge_2$ [63], and Gd_2PdSi_3 [60].

IV. DISCUSSION

We have introduced the concept of spin-flux carrying skyrmions as a possible additional modality for magnetic memory in spintronics. Spin-flux has its origin in the fundamental two-valued nature of the wave function of spin − 1/2 electrons. Under a 2π rotation in its internal coordinate system, the electron wave function changes sign, leading to observable physical consequences. We have derived the explicit SU(2) gauge field for spin-flux skyrmions and demonstrated how their emergent fields and Hall response differ fundamentally from conventional skyrmions. The monopolar σ_x component inherent to spin-flux skyrmions generates a finite average emergent field, leading to an additional contribution to the topological Hall conductivity that is absent in conventional systems. This feature provides a possible interpretation of several experimentally observed Hall resistivity behaviors that cannot be fully explained by the conventional skyrmion model.

The tunability of the Hall response with respect to spin polarization indicates that spin-flux skyrmions could be used to control charge transport in a manner not accessible with conventional textures. For instance, the Hall conductivity in such systems can be enhanced or suppressed depending on the spin alignment of itinerant electrons, offering a controllable mechanism for transverse charge flow under a longitudinal current. Such behavior has potential relevance for memory and logic architectures based on skyrmion motion, where controlling transverse deflection is essential to reduce energy dissipation and improve device stability [7,18,65,66].

Spin-flip scattering [67,68] provides another probe to identify skyrmionic spin textures. In most experimental conditions, the kinetic energy of conduction electrons is significantly larger than the characteristic energy scale of the skyrmion–electron interaction. Previous theoretical works [69,70] have treated this interaction as a scattering potential and analyzed the corresponding scattering amplitudes as a function of relevant system parameters. Spin-flux skyrmions lead to stronger forms of spin-flip scattering of conduction electrons, than realized by conventional skyrmions. This is apparent from the presence of finite off-diagonal components in the spin-flux skyrmion gauge field, absent in the conventional case. The observation of (stronger than conventional) spin-flip scattering may provide additional support for the presence of spin-flux skyrmions.

The physical origin of the spin-flux skyrmion is related to the structure of the many-electron wave function underlying the magnetic texture. The local magnetic moments are quantum expectation values with respect to a wave function built from spin-1/2 electrons, whose two-valued nature is essential. When the electronic wave function is followed around a closed path encircling the skyrmion, its internal spinor undergoes a full 360° rotation. This results in a sign change corresponding to a spin-flux of π [34,37,71]. This internal rotation may be driven by spin-orbit interactions, such as the Dzyaloshinkii-Moriya interaction [20]. A full energetic comparison between spin-flux and conventional skyrmions, requiring a quantum many-body analysis, is a worthy direction for future study.

Spin-flux skyrmions are a direct consequence of the doubly connected topological structure of the group manifold of physical rotations in three-dimensional space. We hope that our exposition will motivate more focused experimental effort to identify such skyrmions. Such an identification may offer previously unrecognized technological opportunities in spintronics.

ACKNOWLEDGMENTS

This work was supported by the Natural Sciences and Engineering Research Council of Canada.

DATA AVAILABILITY

The data that support the findings of this article are not publicly available. The data are available from the authors upon reasonable request.

APPENDIX A: DETAILED CALCULATION OF EMERGENT MAGNETIC FIELD

The emergent vector potential and the corresponding magnetic field arising from the SU(2) gauge transformation are expressed as

$$\vec{\mathcal{A}} = -i\hbar U^\dagger \nabla U, \vec{B} = \nabla \times \vec{\mathcal{A}}. \tag{A1}$$

1. Conventional skyrmion

For a conventional skyrmion, the explicit form of the unitary matrix is $U_1(\boldsymbol{r}) = \exp(-i\frac{\pi(\hat{n}\cdot\vec{\sigma})}{2}) = -i\hat{n}\cdot\vec{\sigma}$, where the unit vector $\vec{n} = (\sin\frac{\theta}{2}\cos\phi, \sin\frac{\theta}{2}\sin\phi, \cos\frac{\theta}{2})$. Here, we have used the Pauli matrix identity $e^{i\theta\hat{n}\cdot\vec{\sigma}} = \sigma_0\cos\theta + i\hat{n}\cdot\vec{\sigma}\sin\theta$. Using the gradient operator $\nabla \equiv \hat{r}\frac{\partial}{\partial r} + \frac{\hat{\zeta}}{r}\frac{\partial}{\partial\zeta}$, the corresponding SU(2) vector potential can be derived using the observation that $\hat{n}\cdot\vec{\sigma}\,\partial_r(\hat{n}\cdot\vec{\sigma}) = \frac{\theta_r}{2}\begin{pmatrix}0 & e^{-i\phi}\\ -e^{i\phi} & 0\end{pmatrix}$ and $\hat{n}\cdot\vec{\sigma}\,\partial_\zeta(\hat{n}\cdot\vec{\sigma}) = i\phi_\zeta\begin{pmatrix}\sin^2(\frac{\theta}{2}) & -\frac{1}{2}e^{-i\phi}\sin\theta\\ -\frac{1}{2}e^{i\phi}\sin\theta & -\sin^2(\frac{\theta}{2})\end{pmatrix}$. It follows that

$$\vec{\mathcal{A}} = -i\hbar U_1^\dagger \nabla U_1 \tag{A2}$$

$$\equiv \frac{\hbar}{2}\Bigg[\theta_r(\sigma_y\cos\phi - \sigma_x\sin\phi)\hat{r} + \hat{\zeta}\frac{2\phi_\zeta\sin\frac{\theta}{2}}{r} \times\left(\sigma_z\sin\frac{\theta}{2} - \cos\frac{\theta}{2}(\sigma_x\cos\phi + \sigma_y\sin\phi)\right)\Bigg]. \tag{A3}$$

Consequently, the corresponding emergent magnetic field is given by [7,18]

$$\vec{B} = \nabla\times\vec{\mathcal{A}} \tag{A4}$$

$$= \frac{1}{r}\left[\frac{\partial}{\partial r}(rA_\zeta) - \frac{\partial A_r}{\partial\zeta}\right]\hat{z} \tag{A5}$$

$$= \frac{\hbar}{2r}\theta_r\phi_\zeta\left[\sigma_z\sin\theta + 2\sin^2\frac{\theta}{2}(\sigma_x\cos\phi + \sigma_y\sin\phi)\right]\hat{z}$$

$$\equiv B_z\hat{z}, \tag{A6}$$

where $\theta_r = \frac{\partial\theta}{\partial r}, \phi_\zeta = \frac{\partial\phi}{\partial\zeta}$. We consider a Néel-type skyrmion in our calculation, described by the solution $\theta(r) = 2\tan^{-1}(r/\rho_0)$ and $\phi = \zeta$. With this configuration, the emergent vector potential and the corresponding emergent magnetic field are given by

$$\vec{\mathcal{A}} = \frac{\hbar}{2}\Bigg[\frac{2\rho_0}{r^2+\rho_0^2}(\sigma_y\cos\zeta - \sigma_x\sin\zeta)\hat{r} + \hat{\zeta}\left(\sigma_z\frac{2r}{r^2+\rho_0^2} - \frac{2\rho_0}{r^2+\rho_0^2}(\sigma_x\cos\zeta + \sigma_y\sin\zeta)\right)\Bigg] \tag{A7}$$

$$B_z = \hbar\left[\sigma_z\frac{2\rho_0^2}{\left(r^2+\rho_0^2\right)^2} + \frac{2r\rho_0}{\left(r^2+\rho_0^2\right)^2}(\sigma_x\cos\zeta + \sigma_y\sin\zeta)\right] \equiv \sigma_z B_{zz} + \sigma_x B_{zx} + \sigma_y B_{zy}. \tag{A8}$$

2. Spin-flux skyrmion

For a spin-flux skyrmion, the explicit form of the unitary matrix is $U_2 = \exp(-i\frac{\sigma_z\phi(\zeta)}{2})\exp(-i\frac{\sigma_y\theta(r)}{2})$. The corresponding vector potential can be deduced using the Pauli matrix identity from A 1 and the cyclic algebra $\sigma_j\sigma_k = \delta_{jk}\sigma_0 + i\epsilon_{jkl}\sigma_l$, where ϵ_{jkl} is the antisymmetric Levi-Civita tensor.

$$\vec{\mathcal{A}} = -i\hbar U_2^\dagger\nabla U_2 \tag{A9}$$

$$= -i\hbar\left[\frac{-i\theta_r}{2}\sigma_y\hat{r} + \frac{\hat{\zeta}}{2r}(-i\phi_\zeta)U_2^\dagger\sigma_z U_2\right]. \tag{A10}$$

It is straightforward to show that $U_2^\dagger\sigma_z U_2 = \sigma_z\cos\theta - \sigma_x\sin\theta$.

It follows that

$$\vec{\mathcal{A}} = \frac{\hbar}{2}\left[-\theta_r\sigma_y\hat{r} + \frac{\zeta\hat{\phi}_\zeta}{r}(-\sigma_z\cos\theta + \sigma_x\sin\theta)\right]. \tag{A11}$$

Consequently, the corresponding emergent magnetic field is given by

$$\vec{B} = \nabla\times\vec{\mathcal{A}} \tag{A12}$$

$$= \frac{1}{r}\left[\frac{\partial}{\partial r}(rA_\zeta) - \frac{\partial A_r}{\partial\zeta}\right]\hat{z} \tag{A13}$$

$$= \hbar\frac{\theta_r\phi_\zeta}{2r}\left[\sigma_z\sin\theta + \sigma_x\cos\theta\right]\hat{z} \equiv B_z\hat{z}. \tag{A14}$$

We consider a Néel-type skyrmion in our calculation, described by the solution $\theta(r) = 2\tan^{-1}(r/\rho_0)$ and $\phi = \zeta$. With this configuration, the emergent vector potential and the corresponding emergent magnetic field are given by

$$\vec{\mathcal{A}} = \frac{\hbar}{2}\left[-\frac{2\rho_0}{\rho_0^2+r^2}\sigma_y\hat{r} + \hat{\zeta}\left(-\sigma_z\frac{\rho_0^2-r^2}{r\left(\rho_0^2+r^2\right)} + \sigma_x\frac{2\rho_0}{\rho_0^2+r^2}\right)\right]$$

$$\equiv \mathcal{A}_r\hat{r} + \mathcal{A}_\zeta\hat{\zeta} \tag{A15}$$

$$B_z = \hbar\left[\sigma_z\frac{2\rho_0^2}{\left(\rho_0^2+r^2\right)^2} + \frac{\rho_0\left(\rho_0^2-r^2\right)}{r\left(\rho_0^2+r^2\right)^2}\sigma_x\right] \equiv \sigma_z B_{zz} + \sigma_x B_{zx}. \tag{A16}$$

The radial component $\mathcal{A}_r$ contains a σ_y term and is independent of the azimuthal angle ζ, i.e., $\frac{\partial\mathcal{A}_r}{\partial\zeta} = 0$. Therefore, the σ_y component does not contribute to the emergent magnetic field.

APPENDIX B: DERIVATION OF THE SPIN-DEPENDENT LORENTZ EQUATION IN A HOMOGENEOUS MATRIX FIELD

The Hamiltonian of an electron in the presence of an emergent field is

$$H' = \frac{1}{2m}(\boldsymbol{P} + \boldsymbol{\mathcal{A}})^2 - J_h\sigma_z, \tag{B1}$$

where $\boldsymbol{\mathcal{A}}$ is the microscopic synthetic gauge field due to skyrmions. As described earlier, we replace H' with a mean-field Hamiltonian, H_{MF} in which $\boldsymbol{\mathcal{A}}$ is replaced by its configuration averaged value $\boldsymbol{\mathcal{A}}_{av} = [\boldsymbol{\mathcal{A}}]_c$. In the symmetric gauge this becomes

$$\boldsymbol{\mathcal{A}}_{\rm av} = \tfrac{1}{2}B_z^{\rm av}(\vec{r}\times\hat{z}), \tag{B2}$$

where the total averaged emergent magnetic field is given by $B_z^{\rm av} = B_{zx}^{\rm av}\sigma_x + B_{zy}^{\rm av}\sigma_y + B_{zz}^{\rm av}\sigma_z$. For the U_1 skyrmion, we have $B_{zx}^{\rm av} = B_{zy}^{\rm av} = 0$, while for the U_2 spin-flux skyrmion, $B_{zy}^{\rm av} = 0$, but $B_{zx}^{\rm av} \neq 0$. The mean-field Hamiltonian is then given by

$$\begin{aligned} H_{MF} &= \frac{1}{2m}(\boldsymbol{P} + \boldsymbol{\mathcal{A}}_{\rm av})^2 - J_h\sigma_z \qquad \text{(B3)}\\ &= \frac{1}{2m}\Bigg[\sigma_0\left(P_x^2 + P_y^2 + \frac{(x^2+y^2)}{4}\left(B_z^{\rm av}\right)^2\right)\\ &\quad + B_z^{\rm av}(xP_y - yP_x) - J_{1h}\sigma_z\Bigg], \end{aligned}$$

where $J_{1h} = 2mJ_h$ (B4)

$$= \frac{1}{2m}\left[\sigma_0\left(\boldsymbol{P}^2 + \frac{r^2}{4}\left(B_z^{\rm av}\right)^2\right) + B_z^{\rm av}L_z - J_{1h}\sigma_z\right], \tag{B5}$$

where $L_z = xP_y - yP_x$ is the z component of the orbital angular momentum operator. The Heisenberg position and momentum operators satisfy a matrix version of the classical equations of motion [72,73]:

$$\begin{aligned} \frac{dx}{dt} &= \frac{i}{\hbar}[H_{MF}, x] = \frac{1}{2m}\left(2P_x\sigma_0 - B_z^{\rm av}y\right) \Rightarrow P_x\sigma_0\\ &= m\frac{dx}{dt} + B_z^{\rm av}y/2 \qquad \text{(B6)}\\ \frac{dy}{dt} &= \frac{i}{\hbar}[H_{MF}, y] = \frac{1}{2m}\left(2P_y\sigma_0 + B_z^{\rm av}x\right) \Rightarrow P_y\sigma_0\\ &= m\frac{dy}{dt} - B_z^{\rm av}x/2 \qquad \text{(B7)} \end{aligned}$$

$$\frac{dP_x}{dt} = \frac{i}{\hbar}[H_{MF}, P_x] = -\frac{1}{2m}\left(\frac{x\left(B_z^{av}\right)^2}{2} + B_z^{\rm av}P_y\right) \tag{B8}$$

$$\frac{dP_y}{dt} = \frac{i}{\hbar}[H_{MF}, P_y] = -\frac{1}{2m}\left(\frac{y\left(B_z^{av}\right)^2}{2} - B_z^{\rm av}P_x\right). \tag{B9}$$

Substituting Eqs. (B6) and (B7) into Eqs. (B8) and (B9), we obtain

$$\frac{dP_x}{dt} = -\frac{1}{2}B_z^{\rm av}\frac{dy}{dt} \tag{B10}$$

$$\frac{dP_y}{dt} = \frac{1}{2}B_z^{\rm av}\frac{dx}{dt}. \tag{B11}$$

Since $\vec{P} = m\dot{\vec{r}}$, we obtain the matrix form of the Lorentz force equation

$$m\ddot{\vec{r}} = -B_z^{av}(\vec{v}\times\hat{z}). \tag{B12}$$

[1] T. H. R. Skyrme and B. F. J. Schonland, Proc. R. Soc. London A **260**, 127 (1961).
[2] T. H. R. Skyrme and W. G. Penney, Proc. R. Soc. London A **262**, 237 (1961).
[3] T. Skyrme, Nucl. Phys. **31**, 556 (1962).
[4] S. Muölbauer, B. Binz, F. Jonietz, C. Pfleiderer, A. Rosch, A. Neubauer, R. Georgii, and P. Böni, Science **323**, 915 (2009).
[5] X. Z. Yu, N. Kanazawa, W. Z. Zhang, T. Nagai, T. Hara, K. Kimoto, Y. Matsui, Y. Onose, and Y. Tokura, Nat. Commun. **3**, 988 (2012).
[6] A. Fert, V. Cros, and J. Sampaio, Nat. Nanotechnol. **8**, 152 (2013).
[7] N. Nagaosa and Y. Tokura, Nat. Nanotechnol. **8**, 899 (2013).
[8] R. Juge, N. Sisodia, J. U. Larrañaga, Q. Zhang, V. T. Pham, K. G. Rana, B. Sarpi, N. Mille, S. Stanescu, R. Belkhou, M.-A. Mawass, N. Novakovic-Marinkovic, F. Kronast, M. Weigand, J. Gräfe, S. Wintz, S. Finizio, J. Raabe, L. Aballe, M. Foerster, *et al.*, Nat. Commun. **13**, 4807 (2022).
[9] R. Rajaraman, *Solitons and Instantons: An Introduction to Solitons and Instantons in Quantum Field Theory* (North-Holland, 1987).
[10] S. Bera and S. S. Mandal, Phys. Rev. Res. **1**, 033109 (2019).
[11] S. Bera and S. S. Mandal, J. Phys.: Condens. Matter **33**, 255801 (2021).
[12] S. Bera, J. Phys.: Condens. Matter **36**, 195805 (2024).
[13] N. Romming, C. Hanneken, M. Menzel, J. E. Bickel, B. Wolter, K. von Bergmann, A. Kubetzka, and R. Wiesendanger, Sci. **341**, 636 2013.
[14] M. Hervé, B. Dupé, R. Lopes, M. Böttcher, M. D. Martins, T. Balashov, L. Gerhard, J. Sinova, and W. Wulfhekel, Nat. Commun. **9**, 1015 (2018).
[15] X. Yu, D. Morikawa, T. Yokouchi, K. Shibata, N. Kanazawa, F. Kagawa, T.-h. Arima, and Y. Tokura, Nat. Phys. **14**, 832 (2018).
[16] X. Z. Yu, N. Kanazawa, Y. Onose, K. Kimoto, W. Z. Zhang, S. Ishiwata, Y. Matsui, and Y. Tokura, Nat. Mater. **10**, 106 (2011).
[17] C. Moreau-Luchaire, C. Moutafis, N. Reyren, J. Sampaio, C. A. F. Vaz, N. Van Horne, K. Bouzehouane, K. Garcia, C. Deranlot, P. Warnicke, P. Wohlhüter, J.-M. George, M. Weigand, J. Raabe, V. Cros, and A. Fert, Nat. Nanotechnol. **11**, 444 (2016).
[18] A. Fert, N. Reyren, and V. Cros, Nat. Rev. Mater. **2**, 17031 (2017).
[19] S. Rohart and A. Thiaville, Phys. Rev. B **88**, 184422 (2013).
[20] I. Dzialoshinskii, Zh. Eksp. Theo. Fiz. **32**, 1547 (1957) [Sov. Phys. JETP **5**, 1259 (1957)].
[21] T. Moriya, Phys. Rev. **120**, 91 (1960).

[22] R. E. Camley and K. L. Livesey, Surf. Sci. Rep. **78**, 100605 (2023).

[23] A. Soumyanarayanan, M. Raju, A. L. Gonzalez Oyarce, A. K. C. Tan, M.-Y. Im, A.. P. Petrovic, P. Ho, K. H. Khoo, M. Tran, C. K. Gan, F. Ernult, and C. Panagopoulos, Nat. Mater. **16**, 898 (2017).

[24] T. Schulz, R. Ritz, A. Bauer, M. Halder, M. Wagner, C. Franz, C. Pfleiderer, K. Everschor, M. Garst, and A. Rosch, Nat. Phys. **8**, 301 (2012).

[25] J. Iwasaki, W. Koshibae, and N. Nagaosa, Nano Lett. **14**, 4432 (2014).

[26] F. Jonietz, S. Mühlbauer, C. Pfleiderer, A. Neubauer, W. Münzer, A. Bauer, T. Adams, R. Georgii, P. Böni, R. A. Duine, K. Everschor, M. Garst, and A. Rosch, Science **330**, 1648 (2010).

[27] H. S. Park, X. Yu, S. Aizawa, T. Tanigaki, T. Akashi, Y. Takahashi, T. Matsuda, N. Kanazawa, Y. Onose, D. Shindo, A. Tonomura, and Y. Tokura, Nat. Nanotechnol. **9**, 337 (2014).

[28] S. S. P. Parkin, M. Hayashi, and L. Thomas, Science **320**, 190 (2008).

[29] M. Beg, R. Carey, W. Wang, D. Cortés-Ortuño, M. Vousden, M.-A. Bisotti, M. Albert, D. Chernyshenko, O. Hovorka, R. L. Stamps, and H. Fangohr, Sci. Rep. **5**, 17137 (2015).

[30] S. Woo, K. M. Song, X. Zhang, Y. Zhou, M. Ezawa, X. Liu, S. Finizio, J. Raabe, N. J. Lee, S.-I. Kim, S.-Y. Park, Y. Kim, J.-Y. Kim, D. Lee, O. Lee, J. W. Choi, B.-C. Min, H. C. Koo, and J. Chang, Nat. Commun. **9**, 959 (2018).

[31] X. Zhang, Y. Zhou, M. Ezawa, G. P. Zhao, and W. Zhao, Sci. Rep. **5**11369 (2015).

[32] I. A. Ado, I. A. Dmitriev, P. M. Ostrovsky, and M. Titov, Phys. Rev. Lett. **117**, 046601 (2016).

[33] N. Rosen, Phys. Rev. **82**, 621 (1951).

[34] S. John and A. Golubentsev, Phys. Rev. B **51**, 381 (1995).

[35] M. Berciu and S. John, Phys. Rev. B **69**, 224515 (2004).

[36] M. Berciu and S. John, Phys. Rev. B **61**, 16454 (2000).

[37] S. John and A. Müller-Groeling, Phys. Rev. B **51**, 12989 (1995).

[38] S. John, M. Berciu, and A. Golubentsev, Europhys. Lett. **41**, 31 (1998).

[39] M. M. Salomaa and G. E. Volovik, Rev. Mod. Phys. **59**, 533 (1987).

[40] H. Kawamura, J. Phys.: Condens. Matter **10**, 4707 (1998).

[41] S. Zhang and S. S.-L. Zhang, Phys. Rev. Lett. **102**, 086601 (2009).

[42] K. Hamamoto, M. Ezawa, and N. Nagaosa, Phys. Rev. B **92**, 115417 (2015).

[43] K. Ohgushi, S. Murakami, and N. Nagaosa, Phys. Rev. B **62**, R6065 (2000).

[44] M. Tomé and H. D. Rosales, Phys. Rev. B **103**, L020403 (2021).

[45] J. Osca and B. Sorée, Phys. Rev. B **102**, 125436 (2020).

[46] J. H. Han, Skyrmions in Condensed Matter in *Springer Tracts in Modern Physics* (Springer, Cham, 2017), Vol. 278.

[47] T. Kasuya, Prog. Theor. Phys. **16**45 (1956).

[48] P. W. Anderson, Phys. Rev. **124**, 41 (1961).

[49] D. Andrikopoulos and B. Sorée, Sci. Rep. **7**, 17871 (2017).

[50] G. Tatara, Physica E **106**, 208 (2019).

[51] N. W. Ashcroft and N. D. Mermin, *Solid State Physics* (Holt, Rinehart and Winston, New York, 1976).

[52] J. Zang, M. Mostovoy, J. H. Han, and N. Nagaosa, Phys. Rev. Lett. **107**, 136804 (2011).

[53] P. Bruno, V. K. Dugaev, and M. Taillefumier, Phys. Rev. Lett. **93**, 096806 (2004).

[54] A. Neubauer, C. Pfleiderer, B. Binz, A. Rosch, R. Ritz, P. G. Niklowitz, and P. Böni, Phys. Rev. Lett. **102**, 186602 (2009).

[55] B. Göbel, A. Mook, J. Henk, and I. Mertig, Phys. Rev. B **95**, 094413 (2017).

[56] Y. Li, N. Kanazawa, X. Z. Yu, A. Tsukazaki, M. Kawasaki, M. Ichikawa, X. F. Jin, F. Kagawa, and Y. Tokura, Phys. Rev. Lett. **110**, 117202 (2013).

[57] A. H. Lone, X. Zou, D. Das, X. Fong, G. Setti, and H. Fariborzi, npj Spintron. **2**, 3 (2024).

[58] A. Matsui, T. Nomoto, and R. Arita, Phys. Rev. B **104**, 174432 (2021).

[59] M. Lee, W. Kang, Y. Onose, Y. Tokura, and N. P. Ong, Phys. Rev. Lett. **102**, 186601 (2009).

[60] T. Kurumaji, T. Nakajima, M. Hirschberger, A. Kikkawa, Y. Yamasaki, H. Sagayama, H. Nakao, Y. Taguchi, T. hisa Arima, and Y. Tokura, Science **365**, 914 (2019).

[61] N. A. Porter, J. C. Gartside, and C. H. Marrows, Phys. Rev. B **90**, 024403 (2014).

[62] S. X. Huang and C. L. Chien, Phys. Rev. Lett. **108**, 267201 (2012).

[63] H. Yoshimochi, R. Takagi, J. Ju, N. D. Khanh, H. Saito, H. Sagayama, H. Nakao, S. Itoh, Y. Tokura, T. Arima, S. Hayami, T. Nakajima, and S. Seki, Nat. Phys. **20**, 1001 (2024).

[64] N. Kanazawa, Y. Onose, T. Arima, D. Okuyama, K. Ohoyama, S. Wakimoto, K. Kakurai, S. Ishiwata, and Y. Tokura, Phys. Rev. Lett. **106**, 156603 (2011).

[65] A. Manchon, H. C. Koo, J. Nitta, S. M. Frolov, and R. A. Duine, Nat. Mater. **14**, 871 (2015).

[66] B. Göbel, I. Mertig, and O. A. Tretiakov, Phys. Rep. **895**, 1 (2021.

[67] J. Ju, H. Saito, T. Kurumaji, M. Hirschberger, A. Kikkawa, Y. Taguchi, T.-h. Arima, Y. Tokura, and T. Nakajima, Phys. Rev. B **107**, 024405 (2023).

[68] D. Singh, Y. Fujishiro, S. Hayami, S. H. Moody, T. Nomoto, P. R. Baral, V. Ukleev, R. Cubitt, N.-J. Steinke, D. J. Gawryluk, E. Pomjakushina, Y. Ōnuki, R. Arita, Y. Tokura, N. Kanazawa, and J. S. White, Nat. Commun. **14**, 8050 (2023).

[69] K. S. Denisov, I. V. Rozhansky, N. S. Averkiev, and E. Lähderanta, Phys. Rev. Lett. **117**, 027202 (2016).

[70] K. S. Denisov, J. Phys.: Condens. Matter **32**, 415302 (2020).

[71] M. Berciu and S. John, Physica B **296**, 143 (2001), proceedings of the Symposium on Wave Propagation and Electronic Structure in Disordered Systems .

[72] E. M. Chudnovsky, Phys. Rev. Lett. **99**, 206601 (2007).

[73] Y. Yamane and J. Ieda, J. Magn. Magn. Mater. **491**, 165550 (2019).